MICS JOURNAL

Mathematics-in-Industry Case Studies Journal, Volume 3, pp. 19-36 (2011)

Shape Reconstruction Techniques for Optical Sectioning of Arbitrary Objects

K. Kumar M. Pisarenco M. Rudnaya * V. Savcenco S. Srivastava

Abstract. This paper considers the reconstruction of a shape from a stack of images obtained by optical sectioning. To this end we describe three algorithms relying on the scalar optics model of light propagation of which the most involved is the deconvolution approach. This approach produces a sequence of deblurred images. We improve the deconvolution approach by implementing a novel stopping criterion for the iterative process. The performance of the algorithms is illustrated by numerical experiments on microscopic images of biological cells.

Keywords. microscopy, shape reconstruction, optical sectioning, focusing, shape from focus, deblurring; deconvolution; matrix perturbation, Cascadic multiresolution method, Perona-Malik diffusion operator.

1 Introduction

Identification of the exact morphology of microscopic objects, such as biological cells in human blood, is of high practical importance. For instance, 3D shape information can be used to identify the exact cell type. Microscopes can provide an optical sectioning of 3D objects, which is basically a sequence of images with different parts of the object in focus. This technique of optical sectioning is well known from other similar applications, such as fetal ultrasound scanning, skin tomography and CT and NMR scanning. Figure 1 illustrates the detection principle. It consists of a microscope that can be moved automatically in the vertical direction. By moving the camera up and down stepwise and acquiring images for each step, a sequence of images that encodes the entire 3D information of the sample is obtained. Given this sequence of images, the problem is to reconstruct the 3D shape of the object.

For a given position of the microscope, only a slice of the object is in focus and the rest is blurred. The challenge is thus to identify internal depth, contour surfaces as well as small details from the sequence of images.

*Eindhoven University of Technology, P.O. Box 513, 5600 MB Eindhoven, The Netherlands, m.rudnaya@tue.nl

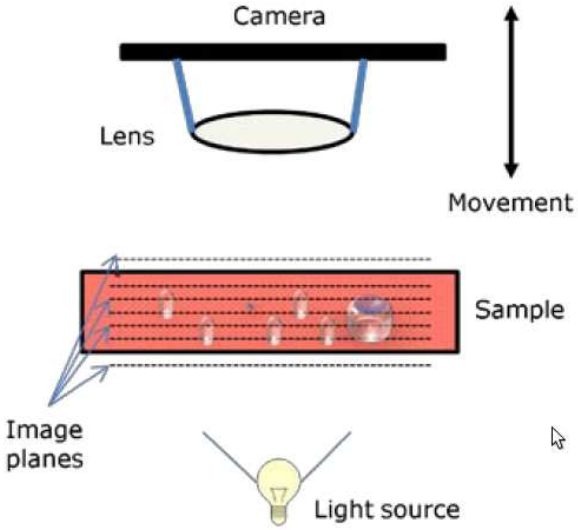

Figure 1: *Illustration of the measurement principle.*

This work deals with identifying the structure of the biological objects, the shape of the complete object as well as the details of the specific structures inside the cell based on the sequence of the images obtained with the microscope. Three approaches are discussed here for recovering different details from these images. The first approach assumes that the geometry is a-priori known and can be parametrized and computes these parameters by comparing the image with the object itself using the image formation model. This approach adopts a forward model approach to solve what is essentially an inverse problem which is often ill-posed in nature. The second approach creates a 3-D reconstruction of the biological object using the stack of images by exploiting the difference between the focused part and the out-of-focus regions in an image. The novelty here is that multiple maxima are being considered instead of single maxima for depth estimation. It is also worth mentioning that the numerical experiments have been conducted using the real experimental pictures. For the third approach, we try to obtain the specific features of the images, for instance, trying to identify a specific structure in an image by deblurring the 2-D image. The input of the algorithm is the image stack at different focus setting and the output is the set of deblurred images. The novelty here is the stopping criterion for the iterative scheme used for deblurring. Again the effectiveness of the stopping criterion has been demonstrated with real experimental pictures. The paper is organized as follows. Section 2 presents the image formation model assumed for this work. Further, we present three possible approaches to the solution of our problem based on the given model. Section 3 is concerned with the reconstruction of easily parametrizable shapes. A Gauss-Newton minimization procedure is used to reconstruct the shape. Section 4 describes a method of obtaining a location-dependent focus measure, which is used afterwards for the estimation of the depth at each pixel position. In Section 5 we review the method described in [16] for the deconvolution of images and

suggest a novel stopping criterion based on the derivative of the regularization term. The discussion and conclusions are presented in Section 7.

2 Image formation model

We use a scalar optics model described in [7] to compute the image acquired by the optical system. The intensity measured by the camera depends on the type of illumination (coherent or incoherent).

Let $\hat{u}(x, y)$ describe a transmittance function, and $\hat{h}(x, y, z)$ describe the intensity of light incident on the object. For coherent light, the image acquired by the charge-coupled device (CCD) camera is then given by the convolution

$$f_z(x, y) = \left|\hat{u}(x, y) * \hat{h}(x, y, z)\right|^2, \tag{1}$$

where $*$ denotes the convolution

$$\hat{u}(x, y) * \hat{h}(x, y, z) := \iint_{\mathbb{R}^2} \hat{u}(x', y')\hat{h}(x - x', y - y', z)dx'dy'.$$

For incoherent light we have

$$f_z(x, y) = |\hat{u}(x, y)|^2 * \left|\hat{h}(x, y, z)\right|^2. \tag{2}$$

Let us define the image intensity of an object as $u(x, y) = |\hat{u}(x, y)|^2$ and the point spread function of the optical device as $h(x, y, z) = \left|\hat{h}(x, y, z)\right|^2$. Then (2) becomes

$$f_z(x, y) = u(x, y) * h(x, y, z). \tag{3}$$

The equation (3) is known as the *linear image formation model*. The point spread function $h(x, y, z)$ of the optical device for a fixed value of $z = z^*$ satisfies

$$\iint_{\mathbb{R}^2} h(x, y, z^*)dxdy = 1. \tag{4}$$

Often a point spread function is modeled by a Gaussian function

$$h(x, y, z^*) = \frac{1}{2\pi\sigma^2(z^*)} e^{-\frac{x^2+y^2}{2\sigma^2(z^*)}}, \tag{5}$$

where the standard deviation $\sigma(z^*)$ is related to the amount of defocus present in the system. In the rest of this paper this image formation model will be referred to as the *forward model*. In the sections 4 and 5 we use the notation f instead of f_z.

3 Reconstruction of simple shapes

We assume that the object being imaged is thin. For instructional purposes we consider a thin cylinder with radius 3 and thickness 0.4, with optical properties described by the following transmittance function

$$\hat{u}(x, y) = e^{(\mathrm{i}\phi - \alpha)c(x,y)}, \tag{6}$$

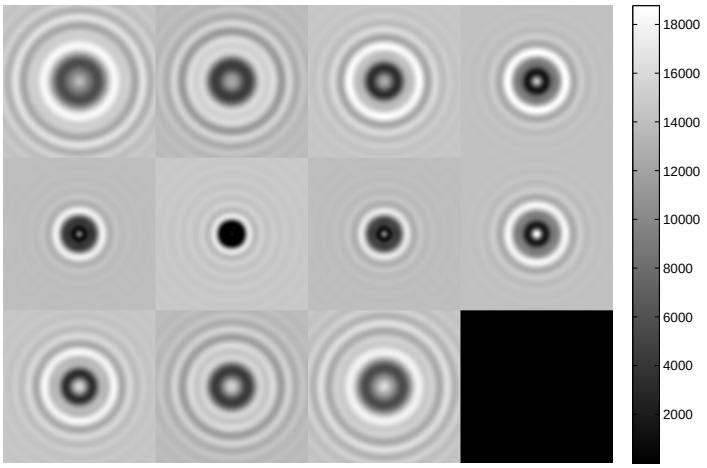

Figure 2: *A stack of images computed at different depths z.*

with

$$c(x,y) = \begin{cases} 1, & \text{if} \quad x^2+y^2 \leq r^2 \\ 0, & \text{otherwise} \end{cases}, \tag{7}$$

where r is the radius of the cylinder, $\phi = 2\pi k\nu$ is the phase, α is a transparency parameter, ν is the thickness and k is a constant which describes the optical properties of the object. The convolution operation for the cylinder described by (6) is performed numerically. An example of a stack of images computed using (1) is shown in Figure 2. The point spread function h of the imaging device is considered to be given. We denote by f_i^{CCD} the stack of images measured by the CCD camera and by f_i^p the images computed with the forward model for a set of shape parameters p. For the cylindrical object, the vector $p = (r, \nu)$ contains two parameters: thickness ν and radius r. We reconstruct the shape by solving the following minimization problem

$$p_{opt} = \underset{p}{\operatorname{argmin}} \sum_{i=1}^{\mathrm{N}} ||f_i^p - f_i^{CCD}||^2. \tag{8}$$

This minimization is performed using the Gauss-Newton algorithm. Figure 3 shows the cost function for two shape parameters: the radius and the thickness of the cylinder. The poly line shows the convergence of the method to the minimum. The iterative process starts from an initial guess $p_0 = (2, 0.3)$, and converges to $p_{opt} = (3, 0.4)$ in less than 10 steps, which coincides with the shape parameters of cylindrical object under consideration.

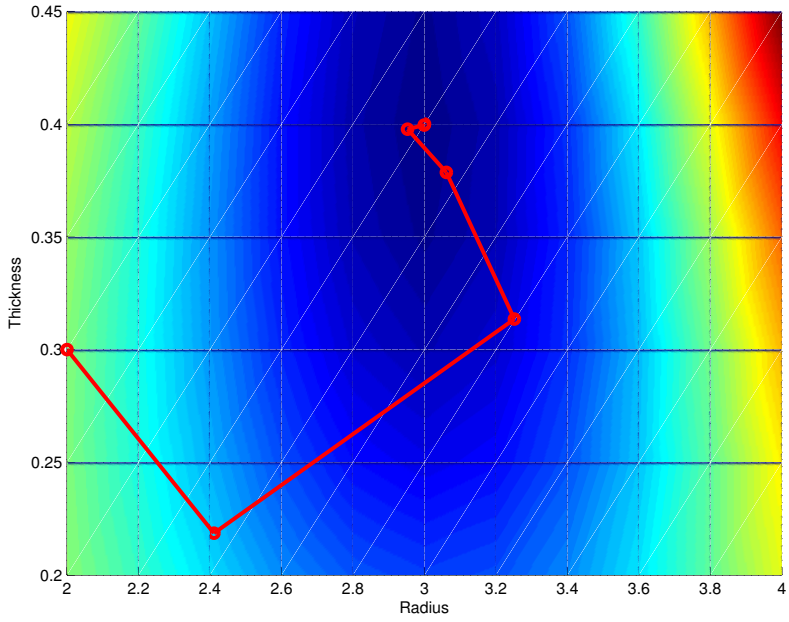

Figure 3: *The cost function.*

4 Shape from focus approach

In this section we solve the shape reconstruction problem using the shape from focus approach described in [17]. This approach uses the focus analysis to compute dense depth maps of rough textured surfaces. Fundamental to the concept of recovering shape from focus analysis is the relationship between focused and defocused images of a scene.

To provide local measures of focus in an image we use the sum-modified-Laplacian (SML) operator

$$\nabla^2_M f = \left|\frac{\partial^2 f}{\partial x^2}\right| + \left|\frac{\partial^2 f}{\partial y^2}\right|. \tag{9}$$

The application of SML in [17] is based on the assumption of the linear image formation model (3) and a Gaussian shape of the point spread function (5). Note that due to the use of the absolute values, the SML is not a linear operator and cannot be implemented as a convolution. However, it can be computed using a simple algorithm. The discrete approximation for the SML operator is given by

$$\begin{aligned} l(x,y) &= |f(x-\Delta x,y) - 2f(x,y) + f(x+\Delta x,y)|\,/(\Delta x)^2 \\ &+ |f(x,y-\Delta y) - 2f(x,y) + f(x,y+\Delta y)|\,/(\Delta y)^2\,. \end{aligned} \tag{10}$$

In order to accommodate for possible variations in the size of texture elements, we compute the

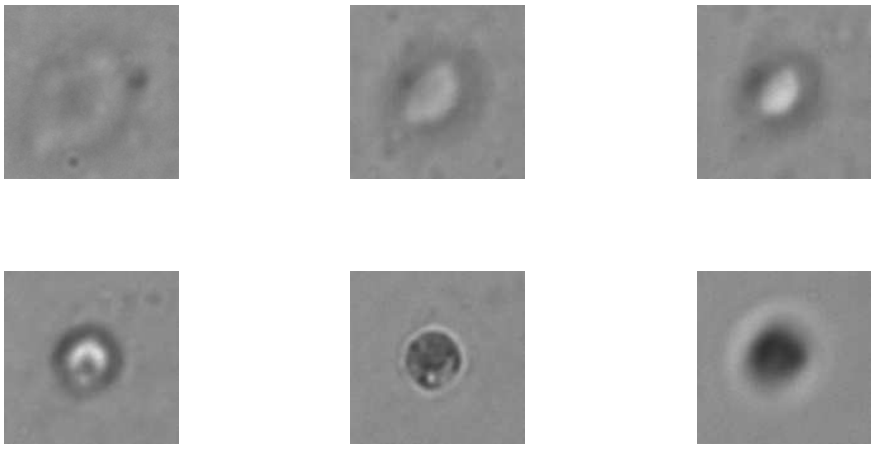

Figure 4: *A sequence of images for a methylene-blue stained white blood cell.*

partial derivatives by using spatial grid sizes Δx and Δy between the pixels employed in the computation of the derivatives.

The focus measure at a grid point (i, j) with coordinates (x_i, y_j) is computed as follows

$$L(i,j) = \sum_{m=-N}^{N} \sum_{n=-N}^{N} \eta_{mn} l(x_i + m\Delta x, y_j + n\Delta y)\,, \tag{11}$$

where

$$\eta_{mn} = \begin{cases} 0, & \text{if} \quad l(x_i + m\Delta x, y_j + n\Delta y) < T_1\,, \\ 1, & \text{otherwise}\,, \end{cases}$$

where T_1 is a threshold parameter and N is a parameter which determines the size of the neighborhood, typically it is $N = 1$ or $N = 2$ and $T_1 = 1$.

We apply the SML operator to the image sequence to obtain a set of focus measures at each image point. For each point (i, j) we estimate the depth d_{ij} by looking for an image for which the correspondent focal measure $L(i, j)$ is maximal compared to the other images. Using the obtained values of the depth for each pixel of the images we can reconstruct the shape.

In [17] only non-transparent objects were considered. For every grid point (i, j) a single SML maxima was found and the corresponding depth d_{ij} was calculated. We extend this approach by considering transparent objects and include and handle the possibility of multiple maxima for a point (i, j), i.e. accepting different depth values $d_{ij}^{(1)}, d_{ij}^{(2)}, \ldots, d_{ij}^{(k)}$.

We test the described method on a sequence of 200 images of white blood cells stained with methylene blue. A small selection of images is presented in Figure 4. We apply the described shape reconstruction technique and obtain the shape presented in Figure 6. In Figure 5 we present a plot of the sequence of focal measures for a fixed pixel. We can see that there are two local maxima which correspond to the upper and lower depth of the cell for the considered pixel.

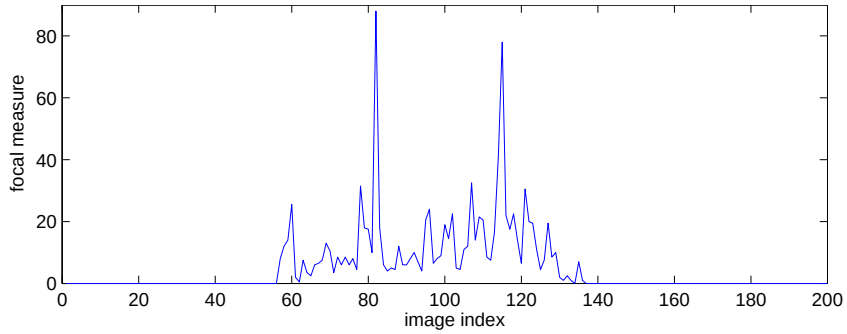

Figure 5: *Plot of the sequence of focal measures for a fixed pixel.*

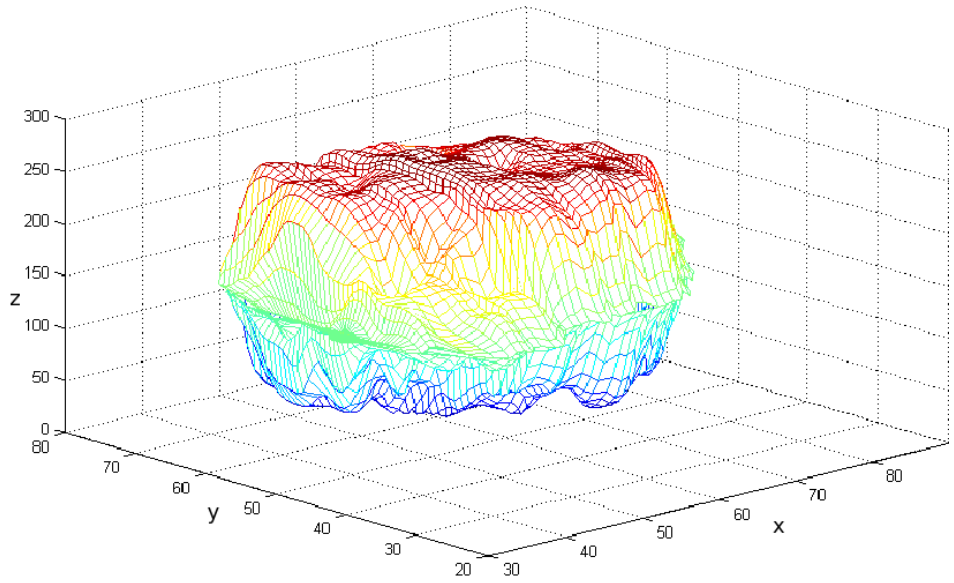

Figure 6: *Shape of the white blood cell.*

Alternative to the SML operator, other focus measures could be used for the same approach. An overview of existing focus measures used in microscopy and other optical applications can be found in [11, 12, 21, 24].

5 Deconvolution approach for the reconstruction of 2D images

In this section we are concerned with obtaining a stack of blur-free images which can later be interpolated in the z-direction in order to obtain the 3D shape.

We add a noise function $\varepsilon(x, y)$ to (3)

$$f(x, y) = u(x, y) * h(x, y, z) + \varepsilon(x, y), \tag{12}$$

which naturally appears in the real-world applications, excluding some applications like artistic painting restoration [19]. Deconvolution is a technique of removing blur from an image. In our case for a given image $f(x, y)$ in (12) the aim is to reconstruct the image $u(x, y)$. The noise function $\varepsilon(x, y)$ is generally unknown.

Blind deconvolution methods, like the APEX method described in [2] and other methods [1, 4, 20], are used when the point spread function $h(x, y, z)$ in (3) is not known; for instance, when it can not be measured or accurately modeled. Instead, a special parametric shape for the point spread function is assumed (such as quasigaussian kernels [2, 20]). We assume that the point spread function is given as a discrete matrix, since it can be accurately measured in modern microscopy. The idea is then to construct a sequence of deblurred images using different point spread functions for the different values of z and then construct the 3D object using this stack of images.

Non-iterative deconvolution approaches, like the APEX method [2], the methods based on the Wiener filter [23] or the concept of minimum norm solutions [10], use the image Fourier transform. In general, the non-iterative deconvolution approaches operate faster, than iterative methods, such as [1, 3, 16, 20, 25], which can be particularly time consuming for large images. However, they are more sensitive to noise in the images than the iterative ones.

In order to perform deconvolution for (12), assuming that the point spread function is given, we follow the cascadic multiresolution method [16], where the deconvolution is combined with a denoising technique.

5.1 Discretization

The discrete image matrix $\mathbf{F} \in \mathbb{R}^{n\times n}$ has been rewritten as a vector $\mathbf{f} \in \mathbb{R}^N$, where $N = n^2$. We discretize (12) in order to obtain a matrix vector equation

$$\mathbf{A}\mathbf{u} + \mathbf{e} = \mathbf{f}, \quad \mathbf{A} \in \mathbb{R}^{N\times N}, \quad \mathbf{u}, \mathbf{f}, \mathbf{e} \in \mathbb{R}^N. \tag{13}$$

The discrete noise function is represented by $\mathbf{e} \in \mathbb{R}^N$. Vector $\mathbf{u} \in \mathbb{R}^N$ in (13) is unknown. The problem is then to find the image $\mathbf{u}$ for the given $\mathbf{A}$ and right hand side vector $\mathbf{f}$. The background and the details for the discretization of (12) and the discussion on the implementation of the boundary conditions can be found in [9]. Here we just provide a brief overview of the method.

Let $\mathbf{H} \in \mathbb{R}^{n\times n}$ be the discrete point spread function. We construct the vector $\mathbf{h} = (h_i)_{i=1}^N \in \mathbb{R}^N$

from the columns of $\mathbf{H}$. For $m = \lfloor \frac{N}{2} \rfloor$ the matrix $\mathbf{A}$ is a Toeplitz matrix

$$\mathbf{A} = \begin{pmatrix} h_m & h_{m-1} & h_{m-2} & \dots & \dots & 0 \\ h_{m+1} & h_m & h_{m-1} & \dots & & \vdots \\ h_{m+2} & h_{m+1} & \ddots & \ddots & \ddots & \vdots \\ \vdots & \ddots & \ddots & \ddots & h_{m-1} & h_{m-2} \\ \vdots & & \ddots & h_{m+1} & h_m & h_{m-1} \\ 0 & \vdots & \vdots & h_{m+2} & h_{m+1} & h_m \end{pmatrix}. \tag{14}$$

In order to satisfy the point spread function normalization property (4) the matrix $\mathbf{A}$ should be column stochastic.

If we neglect $\mathbf{e}$ in (13), then the system can often be efficiently solved with a direct solver. However, when the noise is non-zero, the straightforward application of direct methods results in incorrect solutions. For the linear model (13) the matrix $\mathbf{A}$ is generally ill-conditioned. For this reason a small perturbation (e.g. in the event of presence of noise) in the right hand side results in a large error in the solution $\mathbf{u}$.

One approach is to apply the perturbation methods, and then solve (13) using iterative techniques for linear systems. This implies that we construct another perturbed matrix $\tilde{\mathbf{A}}$, which is obtained as

$$\tilde{\mathbf{A}} = \mathbf{A} + \epsilon \mathbf{I}, \tag{15}$$

where ϵ is a small positive number. For the perturbed matrix $\tilde{\mathbf{A}}$, we have the following result from [22]

$$\frac{||\tilde{\mathbf{u}} - \mathbf{u}||}{||\mathbf{u}||} \leq \epsilon ||\mathbf{A}^{-1}||, \tag{16}$$

where $\mathbf{A}^{-1}$ is the inverse of matrix $\mathbf{A}$. Relation (16) basically provides us the information that the relative error in the solution is bounded by the norm of the inverse matrix, or the condition number of the matrix $\mathbf{A}$. However, (16) does not provide any useful information if the condition number of $\mathbf{A}$ becomes large. If the right hand side contains some noise then the solution of the perturbed problem can lead to the magnification in the error by the factor of the norm of inverse of the matrix $\mathbf{A}$, which can be very large. In [8], [15] the appropriate choice of ϵ has been discussed.

5.2 Regularization

For the equation (12) the inverse of the convolution operator, if it exists, is unbounded. We regularize (12) and then approximate the solution of the original problem by that of the regularized problem. For instance, if we use Tikhonov regularization to regularize the equation, we find u such that

$$\int_{\Omega\subset\mathbb{R}^2} \Big(\frac{1}{2}(h*u-f)^2+\alpha R(u)\Big)dxdy, \tag{17}$$

is minimized, where $\alpha>0$ is a regularization parameter and $R(u)$ is a regularization function. The Euler-Lagrange equation associated with (17) satisfies the following partial differential equation in the steady state

$$\frac{\partial u}{\partial t} = -h*(h*u-f)+\alpha D(u), \tag{18}$$

$$u(x,y,0) = f. \tag{19}$$

The diffusion operator $D(u)$ is related to the derivative of $R(u)$. The derivation is provided in Section 5.4 where we derive a relation between the $R(u)$ and the $D(u)$ to propose the stopping criterion. One choice of the non-linear diffusion operator $D(u)$ is the Perona-Malik diffusion operator, which is given by

$$D(u) = \nabla\cdot(\frac{1}{1+\rho|\nabla u|^2}\nabla u), \tag{20}$$

where ρ is a positive constant. We refer to [16] and references therein for further details about the derivation of (18)-(19) and the value choice of parameter α. An extensive discussion on the choice of ρ can be found in [5], [6], [13], [14].

5.3 Time integration

The equation (18) with the initial condition (19) is a non-linear partial differential equation, and can be understood as combining the idea of the non-linear diffusion equation with the matrix vector equation. The steady state solution satisfies the linear equation (12) as well as the non-linear Perona-Malik type diffusion equation presented in [18]. The solution of the non-linear equation (18) leads to the diffusion along the level curves of u and at the same time, steepening of the profile where the gradient is strong. To solve the equation (18), the semi-discrete form can be written as

$$\frac{d\mathbf{u}}{dt} = -\mathbf{A}(\mathbf{A}\mathbf{u}-\mathbf{f})+\alpha\nabla\cdot(\frac{1}{1+\rho|\nabla_d\mathbf{u}|^2}\nabla_d\mathbf{u}), \quad \mathbf{u}(0)=\mathbf{f},$$

where ∇_d denotes the discrete gradient. We apply a modified forward Euler method in which the matrix term $\mathbf{A}(\mathbf{A}\mathbf{u})$ is treated implicitly. The explicit scheme for the diffusion term induces a restriction on the time step size τ. The discrete form for the above equation then takes the form

$$\frac{\mathbf{u}^{n+1}-\mathbf{u}^n}{\tau} = -\mathbf{A}(\mathbf{A}\mathbf{u}^{n+1}-\mathbf{f})+\alpha\nabla\cdot(\frac{1}{1+\rho|\nabla_d\mathbf{u}^n|^2}\nabla_d\mathbf{u}^n),$$

which can be rewritten as

$$(\mathbf{I}+\tau\mathbf{A}^2)\mathbf{u}^{n+1} = \tau\mathbf{A}\mathbf{f}+\alpha\tau\nabla\cdot(\frac{1}{1+\rho|\nabla_d\mathbf{u}^n|^2}\nabla_d\mathbf{u}^n)+\mathbf{u}^n. \tag{21}$$

To solve the equation (21), we note that the matrix $\mathbf{A}$ is sparse. Thus, efficient iterative solvers may be used, such as the conjugate gradient if $\mathbf{A}$ is symmetric positive definite and the GMRES for a non symmetric $\mathbf{A}$. As in [18] and [16], the gradient $\nabla_d \mathbf{u}^n$ is approximated by finite differences of each pixel in the image with the neighborhood pixels. The finite difference in the North-East direction is obtained for instance by convolution of the image with the matrix

$$\mathbf{G}_{NE} = \frac{1}{\sqrt{2}} \begin{bmatrix} 1 & 0 & 0 \\ 0 & -1 & 0 \\ 0 & 0 & 0 \end{bmatrix},$$

the finite difference in the North direction is obtained by convolution of the image with the matrix

$$\mathbf{G}_{N} = \begin{bmatrix} 0 & 1 & 0 \\ 0 & -1 & 0 \\ 0 & 0 & 0 \end{bmatrix}.$$

Similarly, the finite differences in the North-East, East, West, South, South-East and South-West are obtained. Observe that we use the factor $1/\sqrt{2}$ for the diagonal directional derivatives to take care of the different distances between the neighboring pixels for the diagonal and vertical/horizontal directions. To compute $\nabla \cdot (\frac{1}{1+\rho|\nabla_d \mathbf{u}^n|^2} \nabla_d \mathbf{u}^n)$, we again take the convolution of $\frac{1}{1+\rho|\nabla_d \mathbf{u}^n|^2} \nabla_d \mathbf{u}^n$ with the appropriate matrices.

5.4 Stopping criterion

The stopping criterion used in [16] proves to be suboptimal for our purpose. In this section we introduce a new stopping criterion. In order to derive it, we use the structure of the original minimization problem (17) and obtain the equivalent $R(u)$ for the Perona-Malik choice of the diffusion operator. $D(u)$ is obtained from the Euler-Lagrange equation of the minimization problem (17). To obtain $R(u)$ for the given choice of Perona-Malik diffusion operator, we first assume the regularization parameter $R(u)$ of the form

$$R(u) = \psi(|\nabla u|^2).$$

Since we obtain $D(u)$ using the Euler-Lagrange equation of minimization problem (17), we compute the directional derivative of $R(u)$. Hence,

$$R_v(u) = \lim_{\tau \to 0} \frac{\psi(|\nabla u + \tau \nabla v|^2) - \psi(|\nabla u|^2)}{\tau}.$$

Using Taylor expansion for ψ around $|\nabla u|^2$ and taking limit $\tau \to 0$ provides us

$$R_v(u) = \psi(|\nabla u|^2) + 2\psi'(|\nabla u|^2)(\nabla u, \nabla v) - \psi(|\nabla u|^2).$$

Using linearity of inner product and partial integration, we obtain

$$D(u) = \nabla \cdot (g(|\nabla u|^2) \nabla u).$$

where $g(t)$ is a smooth function and is related to $\psi(t)$ as $g(t) = \frac{d\psi}{dt}$. For the Perona-Malik choice of diffusion operator, we have

$$g(t) = \frac{1}{1+\rho t}.$$

An elementary computation shows that

$$\psi(t) = \frac{1}{\rho}\ln(1+\rho t),$$

and hence,

$$R(u) = \frac{1}{\rho}\ln(1+\rho|\nabla u|^2).$$

Following the algorithm given by the numerical scheme (21), it is observed in practice that for a certain value of n artificial artifacts start appearing [16]. As a result, the diffusive term $||R(u)||$ starts increasing with a rate that is higher than the rate observed during the sharpening of the profile. This suggests that the time derivative of $||R(u)||$ can serve as a useful quantity for determining the stopping criterion. Another measure is $||\mathbf{Au}-\mathbf{f}||$ and we can fix the stopping point at the minimum of the quantity

$$S(\mathbf{u}) = (1-\gamma)||\mathbf{Au}-\mathbf{f}|| + \gamma\{\frac{d||R(\mathbf{u})||}{dt}\}^2, \tag{22}$$

where $\gamma \in (0,1)$. $S(\mathbf{u})$ provides a weighted average of the two different stopping criteria. In practice, we compute $\frac{1}{\tau}||R(\mathbf{u}^{n+1})|| - ||R(\mathbf{u}^n)||$ to approximate $\frac{d||\mathbf{R}(u)||}{dt}$ and $||\mathbf{Au}^{n+1}-\mathbf{f}||$ to approximate $||\mathbf{Au}-\mathbf{f}||$.

6 Results of numerical experiments

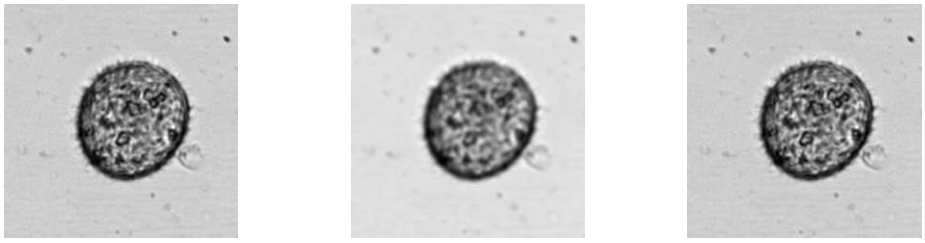

(a) (b) (c)

Figure 7: *(a) Experimental microscopic image. (b) Image blurred with Gaussian PSF. (c) Image deblurred with the direct solver.*

Numerical experiments are conducted on the microscopic images of cells (Figure 7(a)). The image dimensions are 263×263 pixels. First the image is blurred with a Gaussian point spread function (5) with parameters $\sigma = 10$ and the band $g_0 = 3$. The result of the artificial blur is presented in the Figure 7(b). The artificially blurred Figure 7(b) is successfully deblurred with a direct solver. The result is shown in Figure 7(c). No difference is observed between the initial and the deblurred images.

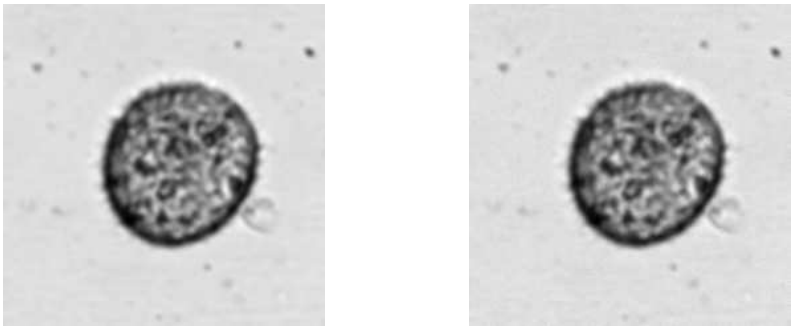

(a) (b)

Figure 8: *(a) Experimental microscopic image 7(a) blurred with the Gaussian point spread function. (b) The same image adorned with noise.*

Next, noise with a relative magnitude of 10^{-2} is applied to the synthetically blurred image. The blurred image with noise corresponds to Figure 8(a). It is difficult to observe the difference between the noise-free Figure 7(b) and the noise Figure 8(a) by naked eye, because the level of noise is relatively low. Figure 9 shows the intensity of the first rows of the two images plotted together, the difference can be observed clearly now.

The direct solver applied to the noisy Figure 8(b) fails (see Figure 10(a)). However, the noisy image deblurred with the perturbed matrix (15) gives much better results (see Figure 10). The perturbation coefficients ϵ used for numerical computations are shown below the images. However, it is not totally clear how the appropriate perturbation coefficient can be estimated prior to the deblurring procedure. Also, we observe that the results of such a deblurring are not satisfactory in a sense that the resulting Figure 12(a) is much closer to the blurred Figure 7(b), as compared to the original (ideal) Figure 7(a).

Further the deblurring and denoising technique based on [16] described in the previous subsections is applied to the blurred image with noise presented in Figure 8(a). The time step size is taken equal to 2 and the diffusion parameter ρ is set to 0.1. The value of α is taken to be 0.5. The amount of iterations is taken equal to 100. Two different stopping criteria are applied to the procedure. The plots of both stopping criteria versus the number of iterations are shown in Figure 11. The

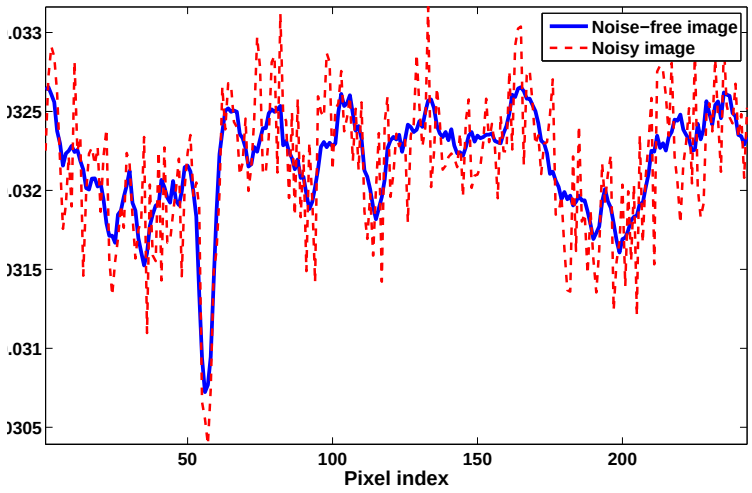

Figure 9: *The first rows of the noise-free image 8(a) and the noisy image 8(b) plotted together.*

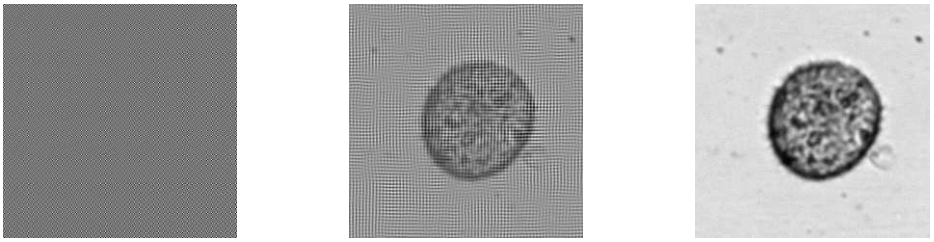

(a) $\epsilon = 0$ (b) $\epsilon = 0.0096$ (c) $\epsilon = 0.1$

Figure 10: *The image deblurred with the perturbation matrix.*

circle on each plot indicates the minimum of each of the stopping criteria, which corresponds to the image that is supposed to be the output of the deblurring procedure.

The norm-based stopping criterion reaches its minimum later (iteration 71), than the derivative-based stopping criterion (iteration 44). The corresponding images are shown in Figure 12. Figure 13 shows the zoomed in parts of the two images. We can see, that the Figure 13(a) has the same amount of fine details like the Figure 13(b). The norm-based stopping criterion indicates the image too late. The Figure 13(a) starts degrading because of noise and small artifacts. The results shown by the derivative-based stopping criterion are more sensitive. The final Figure 12(b) is not completely the same as the ideal Figure 7(a), which is always the case for the real world deblurring. However, it has enough of sharp edges and details to consider this result satisfactory.

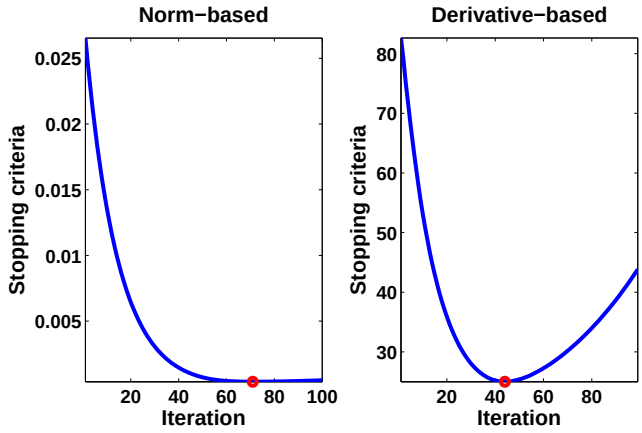

Figure 11: *Two alternative stopping criteria.*

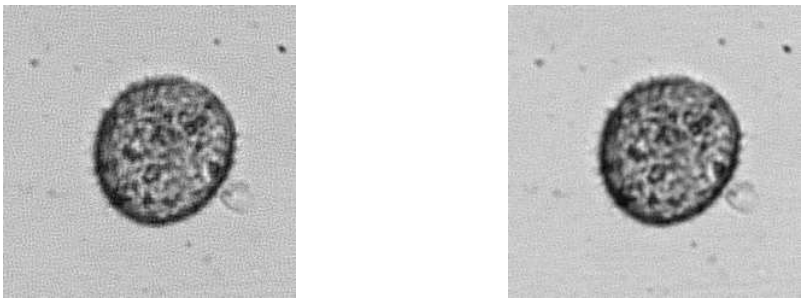

(a) Norm-based stopping criteria: final iteration 71.

(b) Derivative-based stopping criteria: final iteration 44.

Figure 12: *Two images obtained during the iterative deblurring procedure, corresponding to different stopping criteria.*

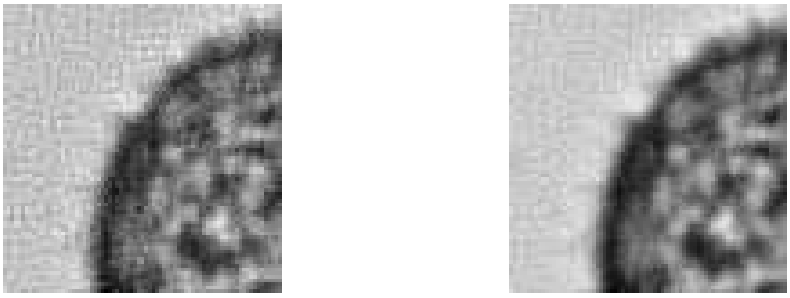

(a) Iteration 71

(b) Iteration 44

Figure 13: *Zoomed in parts of the two images from Figure 12.*

7 Conclusions

Our first approach uses the Gauss-Newton iteration to compute the shape of the 3D object using a stack of images. The limitation of this approach is that the parametrization of the shape is required to be a priori known. This technique can effectively be used for simple shapes and has the advantage that it treats the inverse problem using the forward approach.

For the second approach, for general objects, the Laplacian of the intensity profile provides a good indicator of the depth information and this can be used to reconstruct the object by interpolation techniques.

For the third approach, we deal with blurred and noisy images that are obtained from the optical sectioning of the object using a microscope. An approach to denoise and deblur has been presented based on the work of [16]. The approach is based on the deconvolution of the regularized linear operator. We provide a formulation of the linear operator for any given point spread function and suggest a novel stopping criterion for the iterative deblurring process. This criterion is based on the observation that the continued iteration of the algorithm for denoising and deblurring leads to numerical artifacts, and the rate of change of the regularization term $R(u)$ in the minimization problem (17) provides a good indication of the appearance of the numerical artifacts. Numerical experiments support the effectiveness of this stopping criterion.

Acknowledgments

We would like to thank Unisensor A/S, in particular, N. Agersnap for suggesting the problem, useful discussions and providing us microscopic images for numerical computations. We are also thankful to R.M.M. Mattheij and J.M.L. Maubach for their useful comments and suggestions.

References

[1] D.S.C. Biggs, *Accelerated iterative blind deconvolution*, Ph.D. thesis, University of Auckland, New Zealand, 1998. 26

[2] A. Carasso, *The APEX method in image sharpening and the use of low exponent Lévi stable laws*, SIAM J. Appl. Math. **63** (2002), 593–618. 26

[3] T.F. Chan and K. Wong, *Total variation blind deconvolution*, IEEE Trans. Image Process. **7** (1998), 370–375. 26

[4] J.A. Dobrosotskaya and A.L. Bertozzi, *A Wavelet-Laplace Variational Technique for Image Deconvolution and Inpainting*, IEEE Trans. Im. Proc. **17** (2008), 657–663. 26

[5] S. Esedoḡlu, *An analysis of the Perona-Malik scheme*, Comm. Pure Appl. Math. **54** (2001), 1442–1487. 28

[6] ———, *Stability properties of the Perona-Malik scheme*, SIAM J. Numer. Anal. **44** (2006), 1297–1313. 28

[7] J.W. Goodman, *Introduction to Fourier Optics*, Roberts & Company Publishers, 2005. 21

[8] P.C. Hansen, *Rank-deficient and discrete ill-posed problems: Numerical aspects of linear inversion*, SIAM, Philadelphia, 1998. 27

[9] P.C. Hansen, J.G. Nagy, and D.P. O'Leary, *Deblurring Images : Matrices, Spectra, and Filtering*, SIAM, Philadelphia, 2006. 26

[10] L. Justen and R. Ramlau, *A non-iterative regularization approach to blind deconvolution*, Inverse Prob. **22** (2006), 771–800. 26

[11] E. Krotkov, *Focusing*, Int. J. Comput. Vis. **1** (1987), 223–237. 25

[12] X.Y. Liu, W.H. Wang, and Y. Sun, *Dynamic evaluation of autofocusing for automated microscopic analysis of blood smear and pap smear*, J. Microsc. **227** (1967), 15–23. 25

[13] K. Mikula, *Numerical solution, analysis and application of geometrical nonlinear diffusion equations*, Modern methods in scientific computing and applications, Kluwer Acad. Publ., 2002. 28

[14] ———, *Numerical solution, analysis and application of geometrical nonlinear diffusion equations*, Modern methods in scientific computing and applications, Publishing House of the Slovak University of Technology, 2006. 28

[15] S Morigi, L. Reichel, and F. Sgallari, *An iterative Lavrentiev regularization method*, BIT **43** (2002), 1–14. 27

[16] S. Morigi, L. Reichel, F. Sgallari, and A. Shyshkov, *Cascadic multiresolution methods for image deblurring*, SIAM J. Imaging Sci. **1** (2008), 51–74. 20, 26, 28, 29, 30, 31, 34

[17] S.K. Nayar and Y. Nakagawa, *Shape from Focus*, IEEE Trans. Pattern Anal. Mach. Intell. **16** (1994), 824–831. 23, 24

[18] P. Perona and J. Malik, *Scale-Space and Edge Detection Using Anisotropic Diffusion*, IEEE Trans. Pattern Anal. Mach. Intell. **12** (1990), 629–639. 28, 29

[19] P.D. Romero and V.F. Candela, *Mathematical models for restoration of Baroque paintings*, Lecture Notes in Computer Science, vol. 4179, 2006, pp. 24–34. 26

[20] ———, *Blind Deconvolution Models Regularized by Fractional Powers of the Laplacian*, J. Math. Imaging Vis. **32** (2008), 181–191. 26

[21] M.E. Rudnaya, R.M.M. Mattheij, and J.M.L. Maubach, *Evaluating sharpness functions for automated scanning electron microscopy*, J. Microsc. **240** (2010), 38–49. 25

[22] G.W. Stewart and J.G. Sun, *Matrix Perturbation Theory*, Academic Press, London, 1990. 27

[23] N. Wiener, *Extrapolation, Interpolation, and Smoothing of Stationary Time Series*, The MIT Press, 1964. 26

[24] T.T.E. Yeo, S.H. Ong, Jayasooriah, and R. Sinniah, *Autofocusing for tissue microscopy*, Image Vis. Comput. **10** (1993), 629–639. 25

[25] Y-L. You and M. Kaveh, *A regularization approach to joint blur identification and image restoration*, IEEE Trans. Image Process. **5** (1996), 416–428. 26